Journal of Controlled Release 320 (2020) 83–95

Contents lists available at ScienceDirect

Journal of Controlled Release

journal homepage: www.elsevier.com/locate/jconrel

Hypoxia-sensitive supramolecular nanogels for the cytosolic delivery of ribonuclease A as a breast cancer therapeutic

Xinghui Si[a,b], Sheng Ma[a,b], Yudi Xu[a,d], Dawei Zhang[a,c], Na Shen[a,c], Haiyang Yu[a,c], Yu Zhang[a,c], Wantong Song[a,c,*], Zhaohui Tang[a,b,c,*], Xuesi Chen[a,c]

[a] Key Laboratory of Polymer Ecomaterials, Changchun Institute of Applied Chemistry, Chinese Academy of Sciences, Changchun 130022, PR China
[b] University of Science and Technology of China, Hefei 230026, PR China
[c] Jilin Biomedical Polymers Engineering Laboratory, Changchun 130022, PR China
[d] University of Chinese Academy of Sciences, Beijing 100049, PR China

ARTICLE INFO

Keywords:
Supramolecular
Hypoxia-sensitive
Nanogel
RNase
Protein

ABSTRACT

As the most common malignancy in women, breast cancer causes > 40,000 deaths annually. Ribonuclease A (RNase), a new anti-cancer agent, has attracted intense interest due to its high efficacy and specificity. However, RNase suffers from instability, a short half-life in the circulation and poor membrane penetration. To overcome these challenges, we designed a supramolecular nanogel for the cytosolic delivery of RNase. The nanogels were fabricated using host–guest interactions between azobenzene (Azo) and β-cyclodextrin (βCD) conjugated to poly (L-glutamic acid)-*graft*-poly (ethylene glycol) methyl ether (PLG-*g*-mPEG). RNase could be loaded inside the nanogels in mild aqueous conditions. Following optimization, the RNase-loading content and efficiency of the nanogel were 23.5 wt% and 50.4%, respectively. In the presence of nitroreductase (NTR), the cross-linking point between Azo and βCD was destroyed due to the conformation transition of Azo, ensuring the hypoxia-sensitive release of cargo from the nanogels in tumors in which NTR is overexpressed. *In vitro* release profiles revealed that 75.0% of the RNase was released under hypoxic conditions in 72 h, whilst only 19.7% was released under normoxic conditions. Cytotoxicity assays showed that the RNase-loaded nanogels (nano-RNase) were more efficient in inhibiting the proliferation of 4T1 cells than free RNase. *In vivo* studies showed 68.7% tumor suppression rates (TSR %) in the nano-RNase treated group, whilst free RNase treatment led to a lack of tumor inhibition. To further enhance the hypoxia status of tumors, we combined nano-RNase with a nanoformulation of vascular disrupting agents PLG-*g*-mPEG/combretastatinA4 (nano-CA4) and obtained a TSR of 91.7%. The hypoxia-sensitive supramolecular nanogels provided a versatile platform for the delivery of RNase, highlighting its applicability for cancer therapy.

1. Introduction

Breast cancer is the most common invasive cancer in women and the second leading cause of cancer related death in females, second only to lung cancer [1–2]. In 2019, breast cancer accounted for 30% of all new cancer diagnoses in women. Of all breast cancers, ~10–20% were triple-negative (TNBCs) [3]. TNBC as a highly malignant and poor prognostic breast cancer type is characterized by negativity for estrogen receptors, progesterone receptors, and human epidermal growth factor receptor 2 (HER2) [4,5]. As a result, TNBC does not respond to hormonal therapy or drugs targeting HER2 receptors [6,7]. Surgical resection and chemotherapy are the predominant treatments for breast cancer. However, surgery only holds utility for non-invasive breast cancer, and cytotoxic drug-based chemotherapy is limited by severe side-effects and multidrug resistance in a large proportion of TNBC patients [8]. Protein therapeutics, as a novel mechanism for cancer therapy, holds promise for improved therapeutic effects by virtue of its high specific activity and limited side effects [9–11].

RNase catalyzes the degradation of RNA has been used as an alternative therapeutic drug in clinical trials to treat chemotherapy resistant cancers [12]. Compared to conventional small-molecular drugs, RNase has the advantage of enhanced activity and specificity [13,14]. Moreover, RNase therapy avoids possible multidrug resistance and displays minimal adverse effects [15]. Although RNase shows great

* Corresponding authors at: Key Laboratory of Polymer Ecomaterials, Changchun Institute of Applied Chemistry, Chinese Academy of Sciences, Changchun 130022, PR China.
E-mail addresses: wtsong@ciac.ac.cn (W. Song), ztang@ciac.ac.cn (Z. Tang).

https://doi.org/10.1016/j.jconrel.2020.01.021
Received 24 October 2019; Received in revised form 2 January 2020; Accepted 9 January 2020
Available online 16 January 2020
0168-3659/

promise, many challenges exist in its application for cancer therapy, including low stability, a short circulation half-life, and poor membrane permeability [16,17]. An urgent need for the development of suitable carriers for RNase delivery therefore exists. To address these barriers, chemical modifications for RNase loading into the polymeric carriers can enhance stability and promote cellular uptake [18–20]. Gu et al. [21] developed an *in situ* interfacial polymerization approach for the polymerization of RNase with neutral monomers (acrylamide, AAm), cationic monomers (N-(3-aminopropyl) methacrylamide, APMAAm) and a reduction labile cross-linker (*N*,*N*′-bis(acryloyl)cystamine). The obtained core-shell nanogels could be rapidly endocytosed by tumor cells and released RNase in intracellular reductive conditions, leading to tumor cell death due to RNA degradation. Hennink et al. [22] reported methacrylate-derivatized dextran (dex-MA) nanogels loaded with RNase A for cancer therapy. RNase A was covalently immobilized into the nanogels through disulfide bonds, preventing undesirable release into the extracellular environment and rapid release into the reductive cytosolic environment. The nanogels imparted ~75% loading efficiency and ~20% loading content of RNase A. Though the therapeutic efficiency of RNase A was enhanced using these delivery systems, covalent modifications may result in complex synthesis, reduced protein bioactivity and unanticipated safety concerns [23].

As a novel type of non-covalent interaction, supramolecular self-assemblies are formed at relatively mild conditions, and are suitable for protein entrapment [24]. In addition, supramolecular assemblies reversibly change their structure and shape in response to diverse external environments, which enable the controlled release of entrapped drugs [25–27]. Due to these advantages, supramolecular self-assembly is a promising method of drug delivery, sensing, and tissue engineering. Due to the versatile functions and dynamic regulatory properties, diverse supramolecular platforms have been explored for protein delivery, for example, nanogels, nanoparticles, nanofibers and hydrogels [28–32]. Tseng et al. [33] reported supramolecular nanoparticles as a novel platform to deliver intact transcription factors (TFs). Firstly, TFs were mixed with plasmid DNA which was specifically matched to TF to obtain an anionic TF-DNA complex. Cationic βCD-polyetherimide (βCD-PEI) was then coated onto the surface through electrostatic interactions. Finally, adamantine conjugated PEG (Ad-PEG) was modified on the TF-PEI cores through host-guest interactions between Ad and βCD. *In vitro* studies showed that Cy5-labelled TF-DNA supramolecular nanoparticles exhibited enhanced internalization compared to control groups, suggesting the possibility of supramolecular assemblies for protein drug delivery. Hypoxia, as a common characteristic of solid tumors, occurs due to high oxygen consumption during tumor growth and can be targeted as an effective anti-cancer therapeutic [34].

In this study, a novel supramolecular nanogel formed through the self-assembly of Azo and βCD grafted onto PLG-*g*-mPEG was used for RNase delivery (Scheme 1). RNase could be efficiently loaded into the supramolecular nanogels in mild aqueous conditions and was rapidly released under hypoxic conditions. Both *in vitro* and *in vivo* studies confirmed that the nano-RNase could enhance the therapeutic efficiency of RNase in murine triple-negative breast cancer models. The reported supramolecular nanogels provided a platform for the application of RNase and other protein drugs during cancer therapy.

2. Experimental section

2.1. Materials

RNase, 3-(4,5-dimethyl-thiazol-2-yl)-2,5-diphenyl tetrazolium bromide (MTT) and 4′,6-diamidino-2-phenylindole dihydrochloride (DAPI) were purchased from Sigma-Aldrich. Azobenzene, β-cyclodextrin and N,N-diisopropylethylamine (DIPEA) were purchased from Aladdin Co. Ltd. Genistein and chlorpromazine (CPZ) were bought from Sigma-Aldrich. Cytochalasin B was bought from Solarbio Co. Ltd. 2-(7-azabenzotriazol-1-yl)-*N*,*N*,*N*′,*N*′-tetramethyluronium (HATU) was purchased from J&K chemical Ltd. Tetrahydrofuran (THF), toluene and *N*,*N*-dimethylformamide (DMF) were purchased from Energy Chemicals. Ribonuclease A Detection Kit was purchased from by Sigma-Aldrich (Catalog Number RN0100).

2.2. Methods

GPC analyses of the PLG-*g*-mPEG/Azo and PLG-*g*-mPEG/βCD were performed on a Waters 2414 system (Waters Ultrahydrogel Linear column, 1515 HPLC pump and 2414 Refractive Index detector). The eluents included 0.1 M phosphate buffer (flow rate: 0.5 mL min^{-1}, pH 7.4, 35 °C, poly (ethylene glycol) as a standard). The diameter of the nanogels was determined on a Wyatt QELS instrument with a vertically polarized HeNe laser (fixed angle: 90°, temperature: 25 °C. Transmission electron microscope (TEM) images were obtained from a JEOL JEM-1011 TEM (accelerating voltage: 100 kV). The circular dichroism (CD) spectra were performed on a Chirascan spectrometer (Applied Photophysics Ltd., Leatherhead, UK). Fourier transform infrared (FT-IR) spectra were studied on a Bio-Rad Win-IR instrument using the KBr method.

2.3. Synthesis of PLG-g-mPEG/Azo and PLG-g-mPEG/βCD

The synthesis of PLG-*g*-mPEG/CA4 are shown in supporting information. To obtain PLG-*g*-mPEG/Azo, PLG-*g*-mPEG (1.00 g, 1.88 mmol −COOH) and anhydrous DMF (50 mL) were prepared in 250 mL dried flasks and stirred at room temperature until the PLG-*g*-mPEG dissolved. HATU (550 mg, 1.45 mmol) and DIPEA (933 mg, 7.24 mmol) were then added, and the solution was stirred for 6 h. Azo (285 mg, 1.45 mmol) was then added and the solution was reacted at 30 °C for 48 h in a nitrogen atmosphere. Crude products were dialyzed (MWCO 3500) with deionized water for 3 days and freeze-dried to obtain the product.

Mono-6-deoxy-6-amino-β-cyclodextrin was synthesized as reported in the literature [35]. PLG-*g*-mPEG/βCD was synthesized through a similar method to PLG-*g*-mPEG/Azo.

2.4. Synthesis of RNase-FITC and RNase-Cy5

The RNase was labelled with FITC or Cy5 for quantification. After RNase (100 mg) was dissolved in phosphate buffered saline (PBS, 0.01 M, on phosphate ion basis, pH 7.4), FITC (3.91 mg) or Cy5 (6.83 mg) were added to the RNase and the solution was stirred at room temperature for 24 h. The obtained RNase-FITC or RNase-Cy5 were dialyzed (MWCO 3500 Da) with deionized water and lyophilized.

2.5. Preparation of RNase-loaded nanogels (nano-RNase)

PLG-*g*-mPEG/Azo and PLG-*g*-mPEG/βCD were respectively dissolved in deionized water (5 mL). RNase was dissolved in PB (0.01 M, pH 7.4, 1 mL). Then the three solutions were directly mixed. After vortex for 20 s, the complex was stirred for overnight. Finally, the solution was dialyzed (MWCO 100 kDa) with deionized water for 3 days to remove free RNase. The drug loading content (DLC) and drug loading efficiency (DLE) of nano-RNase were determined using fluorescence spectrometry (λ_{ex} = 488 nm, λ_{em} = 518 nm) according to the following equation:

$$\mathrm{DLC\%} = \frac{\text{weight of protein in protein} - \text{loaded nanogels}}{\text{weight of protein} - \text{loaded nanogels}} \times 100\%$$

$$\mathrm{DLE\%} = \frac{\text{weight of protein loaded in nanogels}}{\text{weight of feeded protein}} \times 100\%$$

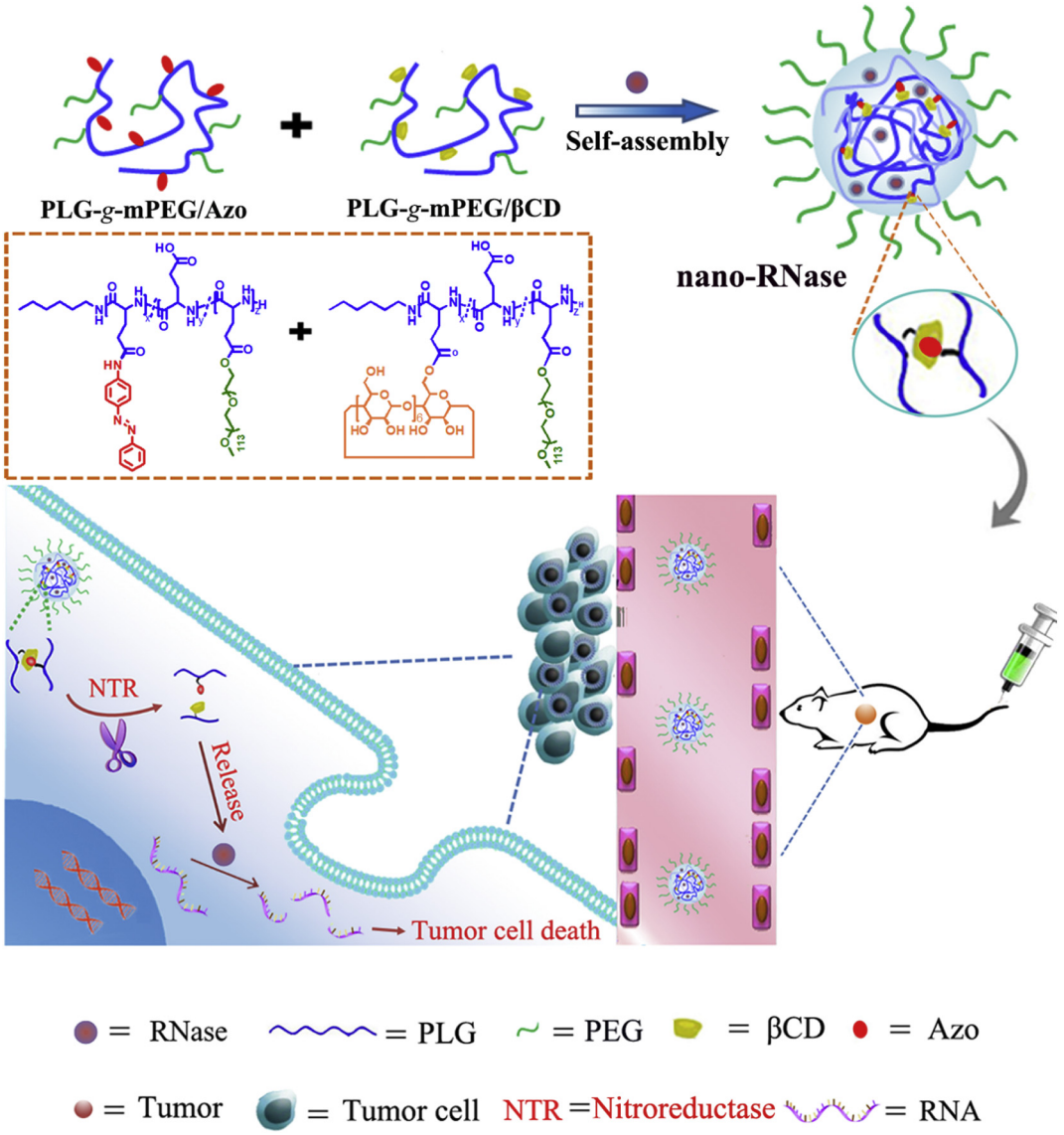

Scheme 1. Schematic illustration of the hypoxia-sensitive nanogels used for RNase delivery. RNase was loaded into the supramolecular nanogels through supramolecular interactions between Azo and βCD grafted onto PLG-*g*-mPEG. Following intravenous injection, the nano-RNase accumulated in tumor tissue by virtue of enhanced permeability and retention (EPR) effects. Following internalization into cancer cells, RNase was released in response to the NTR in tumor cells. This catalyzed the decomposition of RNA promoting tumor cell death.

2.6. Nano-RNase release in vitro

The release behavior of nano-RNase was investigated *in vitro*. RNase was released though dialysis bags (MWCO 100 kDa) incubated in PBS with moderate shaking (90 rpm) at 37 °C. Free RNase was dialyzed in PBS. Nano-RNase was dialyzed under different conditions, including PBS alone (simulating normoxic conditions) and in PBS containing 0.1 mg/mL nitroreductase and 4 mg/mL NADPH (simulating hypoxic condition). At predetermined time points, 100 μL of the released solution was replaced with an equal volume of PBS. Following extraction from the dialysis tube, the solution was deoxygenized through bubbling and the concentration of RNase in the released media was assessed though fluorescence spectrometry.

2.7. Circular dichroism spectrum of released RNase

The secondary structure of free RNase (0.5 mg/mL), RNase-FITC (0.3 mg/mL) and released RNase from the nano-RNase at hypoxic and normoxic conditions at 72 h (concentrations of released RNase in hypoxia and normoxia at 72 h) were 0.17 mg/mL and 0.08 mg/mL, respectively, characterized through circular dichroism (CD) spectroscopy. The spectra of RNase were scanned from 180 to 260 nm at a scanning speed of 1 nm per 10 s. All CD data were expressed as residual ellipticity.

2.8. Cell culture

Mouse mammary tumor cells (4T1) were cultured in Dulbecco's modified Eagle's medium (DMEM) with high glucose containing 10% fetal bovine serum (FBS), 1% penicillin and 1% streptomycin at 37 °C in a 5% CO_2 atmosphere. Hypoxic conditions were achieved by incubating cells in a modular incubator chamber (Billups-Rothenberg, Inc., USA) filled with 1% O_2, 5% CO_2, and 94% N_2.

2.9. Cytotoxicity assay

4T1 cells were used to test the biocompatibility of PLG-*g*-mPEG/Azo and PLG-*g*-mPEG/βCD. Cells were seeded into 96-well plates at a

density of ~7000 cells per well and incubated overnight in 150 μL DMEM. Once the 4T1 cells had adhered to the culture dish, the medium was replaced with 200 μL of fresh DMEM containing different concentrations of PLG-*g*-mPEG/Azo and PLG-*g*-mPEG/βCD. At predetermined time points, 20 μL of MTT was added to the 96-well plates for a further 3 h of incubation. Supernatants were then removed and 150 μL DMSO was added. After shaking for 5 min, absorbances were measured on a Bio-Rad 680 microplate reader at 490 nm. The relative cell viability (%) was calculated using following formula:

$$\text{Cell viability}\ (\%) = (A_{\text{experimental}}/A_{\text{control}}) \times 100$$

$A_{\text{experimental}}$ and A_{control} represent the absorbance of the experimental and control wells, respectively. Data are the average ± SD ($n = 3$). The IC_{50} was defined as the drug concentration causing a 50% loss of cell proliferation.

To verify the hypoxia-responsiveness of nano-RNase, 4T1 cells were treated under normoxic (20%) or hypoxic (1%) conditions at 37 °C in a CO_2-enriched atmosphere for a further 24 h. Cell viability assessments when then performed as described.

2.10. Cellular uptake assays and internalization mechanism

The cellular uptake of nano-RNase was evaluated by flow cytometry and confocal laser scanning microscopy (CLSM). For flow cytometry assays, 4×10^5 4T1 cells per well were seeded into 6-wells plate. After cell adherence, the medium was replaced with fresh DMEM containing nano-RNase-FITC or free RNase-FITC (at a final RNase concentration of 120 μg mL^{-1}). Cells were incubated for a further 3 h or 8 h, washed with PBS (X3) and harvested in trypsin without EDTA and resuspended in PBS. After centrifugation at 1000 rpm for 5 min, cells were washed and resuspended in 0.3 mL PBS and detected on a BD Biosciences flow cytometry.

Cells (2×10^5) were seeded onto glass coverslips in 6-well plates and allowed 24 h to adhere to the culture dish. After overnight incubation for cell adherence, the media was replaced with fresh DMEM containing RNase-FITC or free RNase-FITC at a final RNase concentration of 120 μg mL^{-1}. Cells were incubated for a further 3 or 8 h, washed in 2 mL of PBS (X3), and fixed in 4% formaldehyde for 20 min at room temperature. After washing 3 times, coverslips were placed onto glass microscope slides and fixed using nail polish. The cellular uptake of nano-RNase or free RNase was visualized on a Carl Zeiss LSM 780 confocal microscope.

The internalization mechanism of 4T1 cells was investigated though flow cytometry and confocal microscopy. After pretreated with inhibitors such as cytochalasin D (2.4 μg mL^{-1}), genistein (189 μg mL^{-1}) and CPZ (7 μg mL^{-1}) for 1 h, 4T1 cells were incubation with nano-RNase (RNase was labelled by FITC) for another 4 h. 4T1 cells treated with nano-RNase at 37 °C without any inhibitor were tested as control (100% fluorescence intensity). The internalization of nano-RNase was also conducted at 4 °C to reveal the role of energy.

2.11. Animals

Female Balb/C mice (6–8 weeks old, average body weight 18–20 g) and Wistar rats (200–220 g) were purchased from Beijing Vital River Laboratory Animal Technology Co., Ltd. (Beijing, China). Mice were raised in a specific pathogen free (SPF) animal laboratory. 4T1 cells (2×10^6 per mouse) were injected subcutaneously into the right flank of BALB/c mice to generate the 4T1 TNBC mouse model. All animals received care in compliance with the guidelines outlined in the Guide for the Care and Use of Laboratory Animals. All procedures were approved by the Animal Care and Use Committee of Jilin University.

2.12. Pharmacokinetics

Wistar rats (200–220 g) were randomly divided into two groups ($n = 3$). Free RNase and nano-RNase were administered intravenously *via* the tail vein (4 mg kg^{-1} free RNase-Cy5 or 4 mg kg^{-1} nano-RNase-Cy5 on RNase-Cy5 basis, 4×10^{-4}% injected dose). At defined time points (5, 30, 60, 120, 240, 480, 720 min), blood samples were collected from the orbital cavity. Samples were heparinized and centrifuged to collect the plasma, and the concentration of RNase-Cy5 were determined by fluorescence spectrometry (λ_{ex} = 649 nm, λ_{em} = 670 nm). The half-life of the drug ($t_{1/2}$), area under the drug concentration–time curve from 0 to 12 h in plasma ($AUC_{0\text{-}T}$), total body clearance (CL) and apparent volume of distribution (Vz) were calculated though the PKSolver [36].

2.13. In vivo antitumor efficiency

BALB/c mice bearing 4T1 tumors of approximately 80 mm^3 were prepared as described. Mice were divided into 6 groups randomly, PBS (control), free RNase (10 mg kg^{-1}), blank nanogels (30 mg kg^{-1}), nano-RNase (10 mg kg^{-1} on RNase basis), nano-CA4 (36 mg kg^{-1} on CA4 basis) and nano-CA4 + nano-RNase (10 mg kg^{-1} on RNase basis, 36 mg kg^{-1} on CA4 basis). Free RNase or nano-RNase were injected intravenously *via* the tail vein every other day and nano-CA4 was injected intravenously on day 1. Tumor volumes (V_t), tumor-growth-rates (TGR) and tumor-suppression-rates (TSR %) were calculated using the following equations:

$$\text{Tumor volumes}\ (V_t, \text{mm}^3) = a \times b^2/2$$

$$\text{Tumor} - \text{growth} - \text{rate}\ (\text{TGR}\%) = (V_t/V_0) \times 100\%$$

$$\text{TSR}\% = [(\text{TGRc} - \text{TGRx})/\text{TGRc}] \times 100\%$$

a and b represent the longest and shortest diameter of the tumors measured by a vernier caliper, respectively. V_0 represents the tumor volume on day 0. Subscript c and x represent the control and treatment group, respectively.

Body weights were measured simultaneously every other day to evaluate systemic toxicity. After treatment, mice were sacrificed and the tumors and major organs (heart, liver, spleen, lung and kidney) were excised for histopathological analyses.

2.14. Histological and immunohistochemical analyses

Tumors and major organs were fixed in a 4% formaldehyde overnight and paraffin embedded. Tissues were sectioned (5 μm thickness) and stained with hematoxylin and eosin (H&E) to assess histological alterations. Sections were imaged on a Nikon TE2000U optical microscope.

2.15. Statistical analysis

All experiments were performed on a minimum of three occasion and are expressed as the means ± SD. Data were analyzed for statistical significance using a one-way ANOVA. $p < .05$ were considered statistically significant. ns, not significant. * $p < .05$, ** $p < .01$, *** $p < .001$, **** $p < .0001$.

3. Results and discussion

3.1. Synthesis and characterization of PLG-g-mPEG/Azo and PLG-g-mPEG/βCD

PLG-*g*-mPEG/Azo or PLG-*g*-mPEG/βCD were obtained through the conjugation of Azo and βCD to PLG-*g*-mPEG (Fig. S1). The ^1H NMR spectra of PLG-*g*-mPEG/Azo and PLG-*g*-mPEG/βCD are shown in Fig. 1. For PLG-*g*-mPEG/Azo (Fig. 1A), C_6H_5- (p/q) and $-C_6H_4-$ (m/n) signals in Azo units are at δ 7.6–8.4 ppm. The signals δ 11.5 ppm represent the solvent peak of TFA-d, whilst the signals at δ 4.1 ppm are

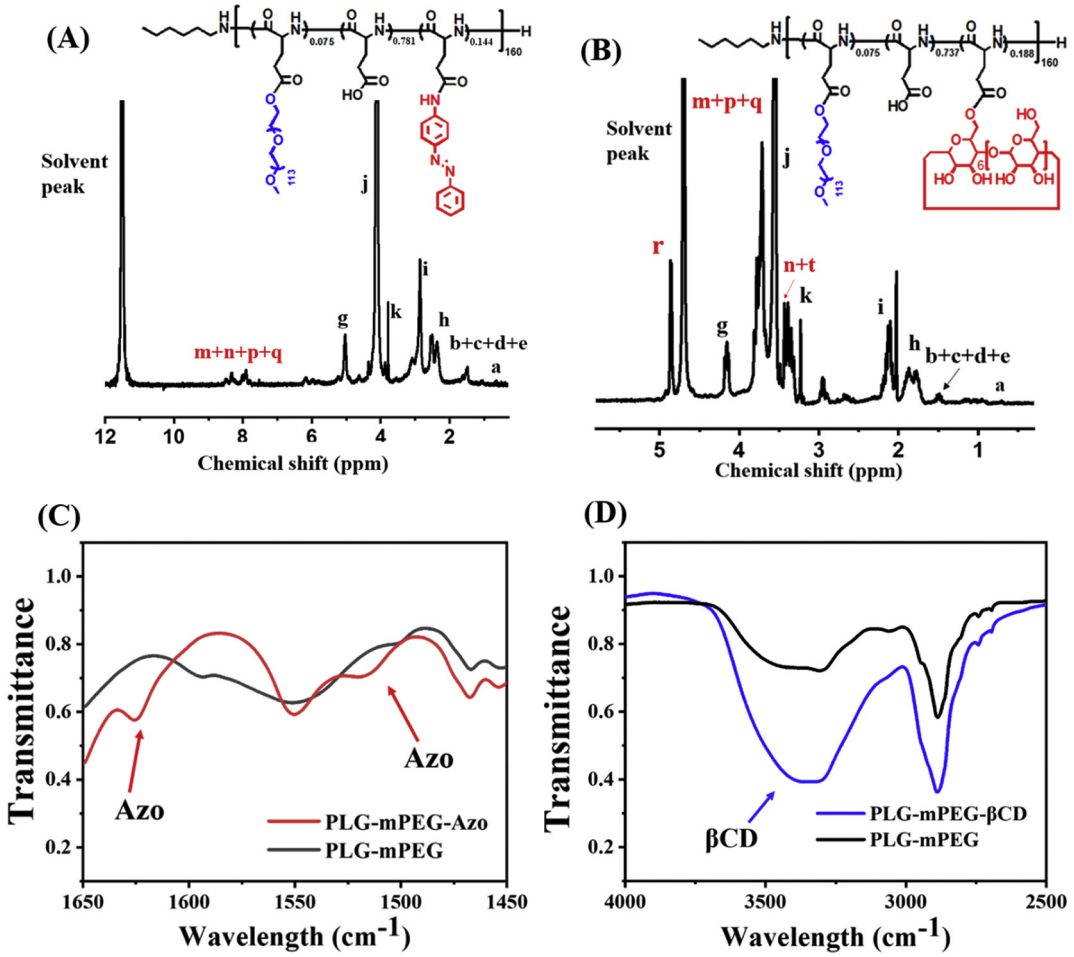

Fig. 1. Characterization of the materials. ^{1}H NMR spectra of PLG-*g*-mPEG/Azo in TFA-d (A) and PLG-*g*-mPEG/βCD in D_2O (B). FT-IR spectra of PLG-*g*-mPEG/Azo (C) and PLG-*g*-mPEG/βCD (D).

$-CH_2CH_2O-$ (j) in PEG units. The signals at δ 5.1 ppm, δ 2.8 ppm and δ 2.3–2.6 ppm are $-CH <$ (g), $-CH_2CO-$ (i) and $-CHCH_2-$ (h) in PLG units, respectively. These data confirmed the successful conjugation of Azo to PLG-*g*-mPEG. Through the assessment of the ratio of C_6H_5- (p/q) and $-CH_2CH_2O-$ (j), the average number of Azo conjugated to PLG chains was 24. Similarly, for PLG-*g*-mPEG/βCD (Fig. 1B), the signals at δ 4.8 ppm (r), δ 3.4 ppm (n), δ 3.0 ppm (t) were characteristic peaks of βCD. Based on the integral area ratio of $-CH <$ (r) and $-CH_2CH_2O-$ (j), the average number of βCD conjugated to PLG chains was 30. To further verify the conjugates of the functional groups to PLG-*g*-mPEG, FT-IR spectra of PLG-*g*-mPEG/Azo and PLG-*g*-mPEG/βCD were measured (Fig. 1C-D). The characteristic peaks of βCD were broad and around 3400 cm^{-1} (−OH stretching band) whilst Azo showed peaks at 1600 ± 20 cm^{-1} and 1500 ± 25 cm^{-1} (−C═C− stretching band) [37,38]. The prominent band around 3400 cm^{-1} was the peak of hydroxyl (O−H stretching), indicating the existence of βCD. The bands at 1625 cm^{-1} and 1525 cm^{-1} were characteristic peaks of Azo, demonstrating its conjugation to the PLG chain. GPC analyses (Fig. S2) showed the number average molecule weight (M_n) of PLG-*g*-mPEG, PLG-*g*-mPEG/Azo and PLG-*g*-mPEG/βCD are 25 × 10^3 Da, 26.8 × 10^3 Da and 28.4 × 10^3 Da, while the poly dispersity index (PDI, Mw/Mn) are 1.15, 1.28 and 1.34, respectively. These results confirm the successful conjugation of Azo and βCD to PLG-*g*-mPEG.

3.2. Preparation of supramolecular nanogels

Supramolecular interactions that occurred between the intermolecular bonds covered the structures and functions of the entities formed by association of two or more chemical species. The interactions developed discrete assemblies and networks of molecules with prescribed properties and functions. The supramolecular interaction between Azo and βCD is typical of the host-guest system, and mainly formed by hydrophobic interactions and hydrogen bonds between Azo and βCD [39]. Based on these interactions, cross-linking networks formed between PLG-*g*-mPEG/Azo and PLG-*g*-mPEG/βCD (Fig. 2A). Different ratios of PLG-*g*-mPEG/Azo and PLG-*g*-mPEG/βCD from 30:0 to 0:30 (*w*/w) were applied for blank nanogels. As shown in Fig. 2B, when the weight ratio of PLG-*g*-mPEG/Azo: PLG-*g*-mPEG/βCD was 30:0, for PLG-*g*-mPEG/Azo alone. The hydrodynamic diameter showed a wide distribution covering 76 nm to 830 nm and low intensities. With the addition of PLG-*g*-mPEG/βCD, the cross-linked networks increased and smaller hydrophobic cores were formed due to hydrophobic interactions and hydrogen bonds between Azo and βCD, with obvious peaks appearing. When the ratio of PLG-*g*-mPEG/Azo: PLG-*g*-mPEG/βCD was 15:15, the diameter of the formed nanogels were the smallest (126 ± 44 nm). As the levels of Azo and βCD coupled to PLG-*g*-mPEG were near, the cross-linking density peaked and the size of the nanogels was smallest at these weight ratios. The continued addition of PLG-*g*-mPEG/βCD resulted in decreased cross-linking density, and increased nanogel size. A ratio of 15:15 was therefore employed. TEM images of the blank nanogels (Fig. 2C) at a weight ratio of 15:15 showed a diameter of 87 ± 10 nm. The assembly behaviour of the blank nanogels under hypoxic conditions were verified by TEM images. As shown in Fig. 2D, the nanogels showed irregular and vague shapes, indicating their disruption. The zeta potential of blank nanogel is −14.7 ± 3.1 mv.

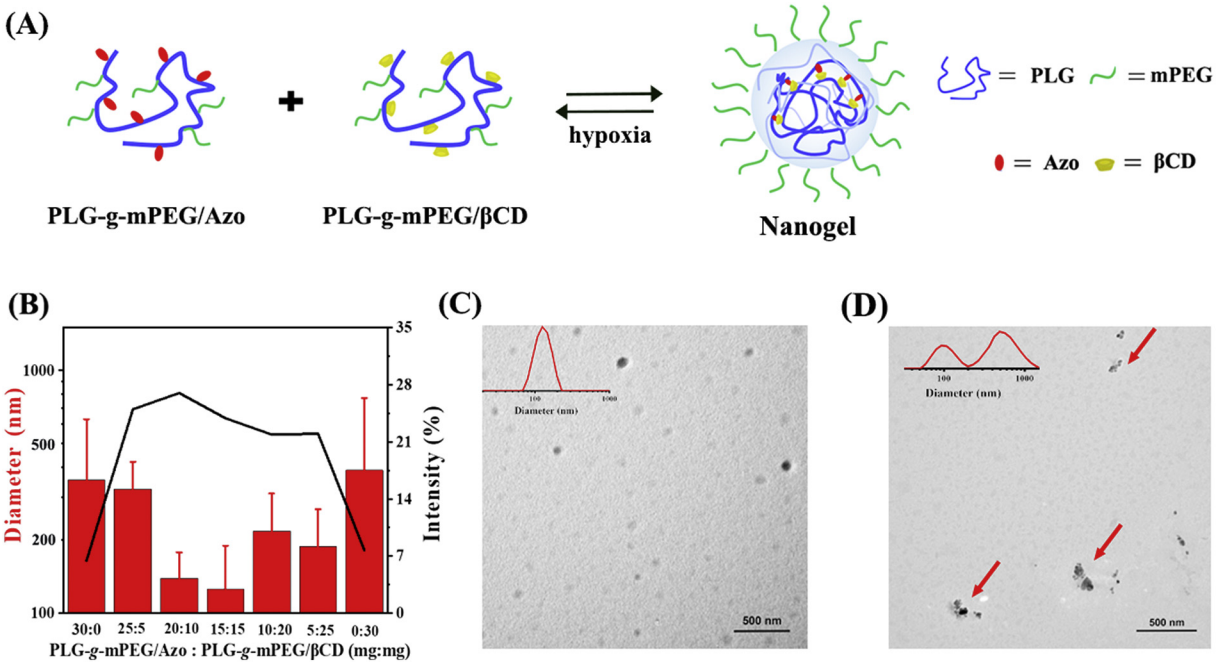

Fig. 2. Size distribution of the blank nanogels at different ratios. (A) Supramolecular self-assemblies. (B) Diameter distribution of blank nanogels at different ratios. (C) TEM images and diameters of the blank nanogels at a weight ratio of 15:15. Scale bar: 500 nm. (D) TEM images and diameters of blank nanogels under hypoxic conditions (0.1 mg/mL of NTR and 4 mg/mL NADPH simulated hypoxic conditions). Red arrows represent the disassembled nanogels. Scale bar: 500 nm. (For interpretation of the references to colour in this figure legend, the reader is referred to the web version of this article.)

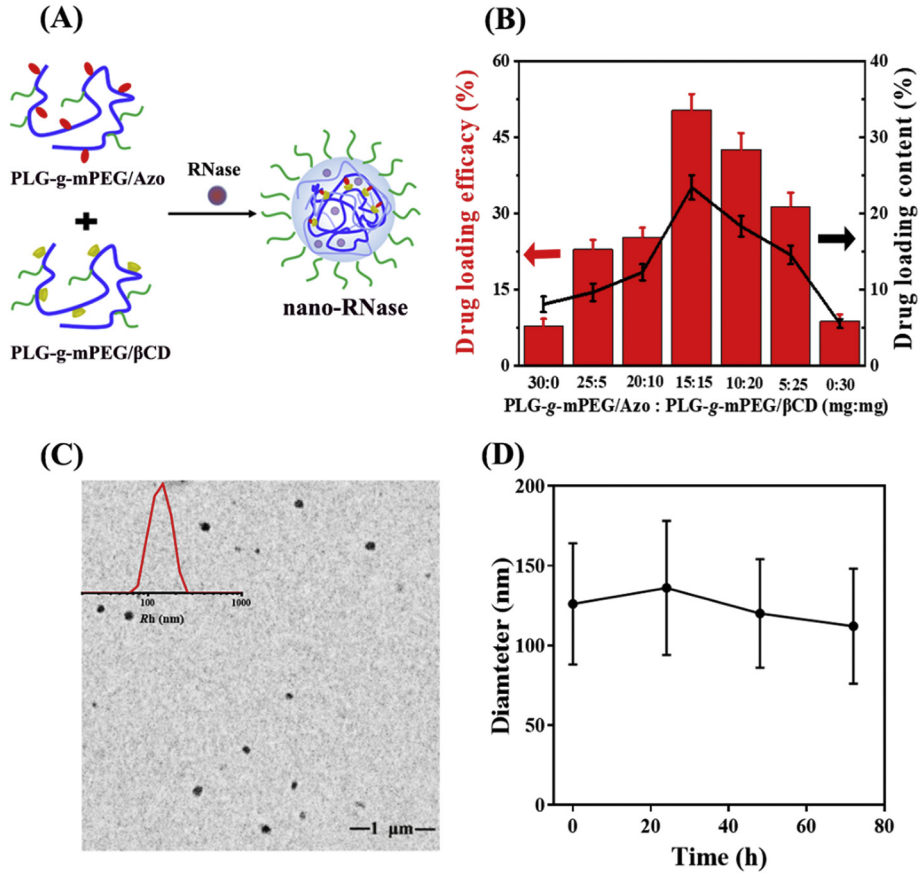

Fig. 3. Characterization of nano-RNase. (A) Self-assembly of nano-RNase. (B) DLC and DLE of RNase at different weight ratios. (n = 3) (C) TEM images and diameters of nano-RNase at a weight ratio of 15:15. Scale bar: 1 μm. (D) Size and intensity of nano-RNase in PBS at 37 °C (n = 3).

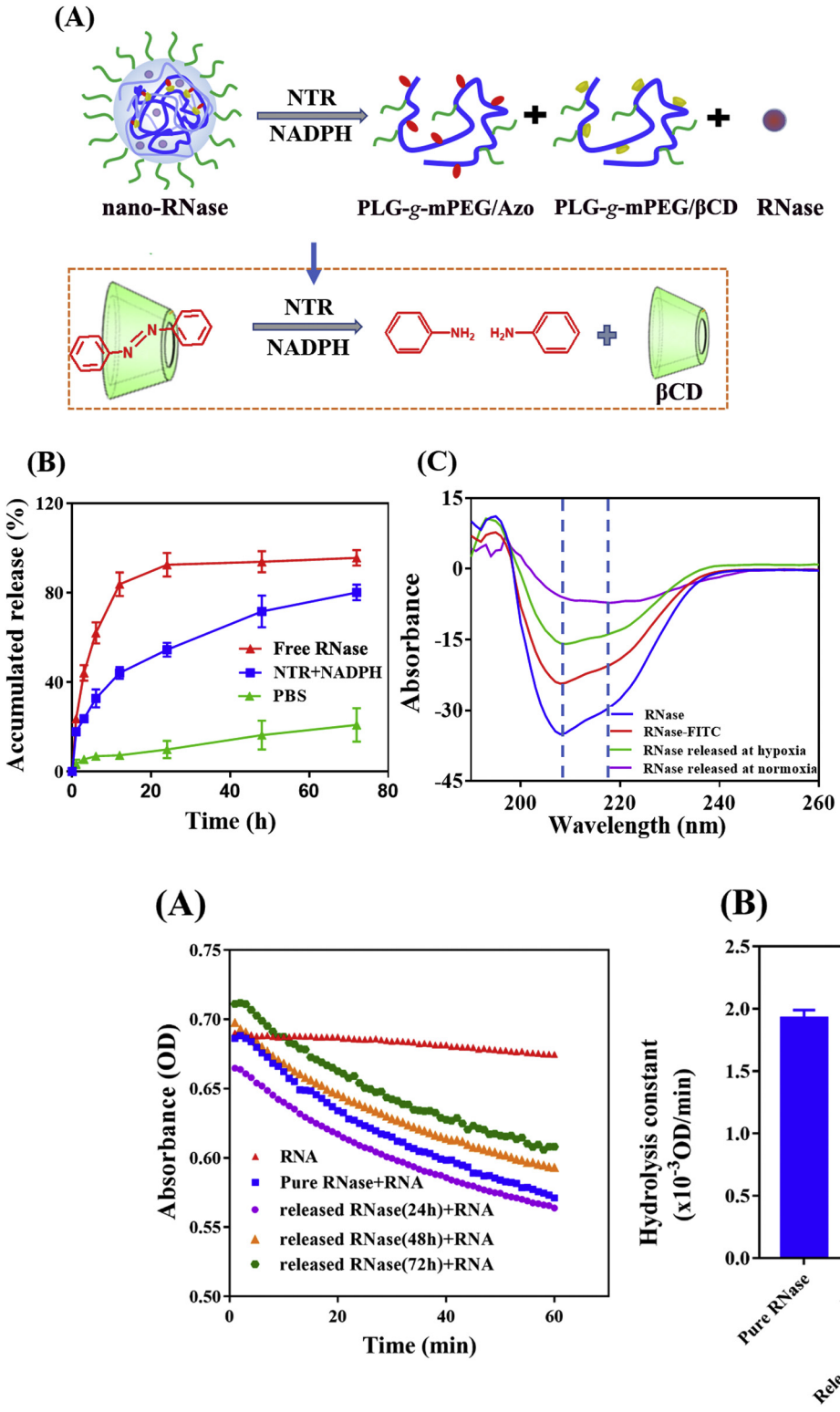

Fig. 4. Release behaviour of nano-RNase and secondary structures of the released RNase *in vitro*. (A) Schematic of the nano-RNase release mechanism. (B) *In vitro* RNase release profiles of nano-RNase in PBS containing 0.1 mg/mL NTR and 4 mg/mL NADPH (n = 3). (C) CD spectra of free RNase (0.5 mg/mL), RNase-FITC (0.3 mg/mL) and released RNase from nano-RNase in hypoxic and normoxic conditions at 72 h (concentration of released RNase at 72 h: 0.17 mg/mL and 0.08 mg/mL, respectively). Each data point indicates represents the average of three independent experiments.

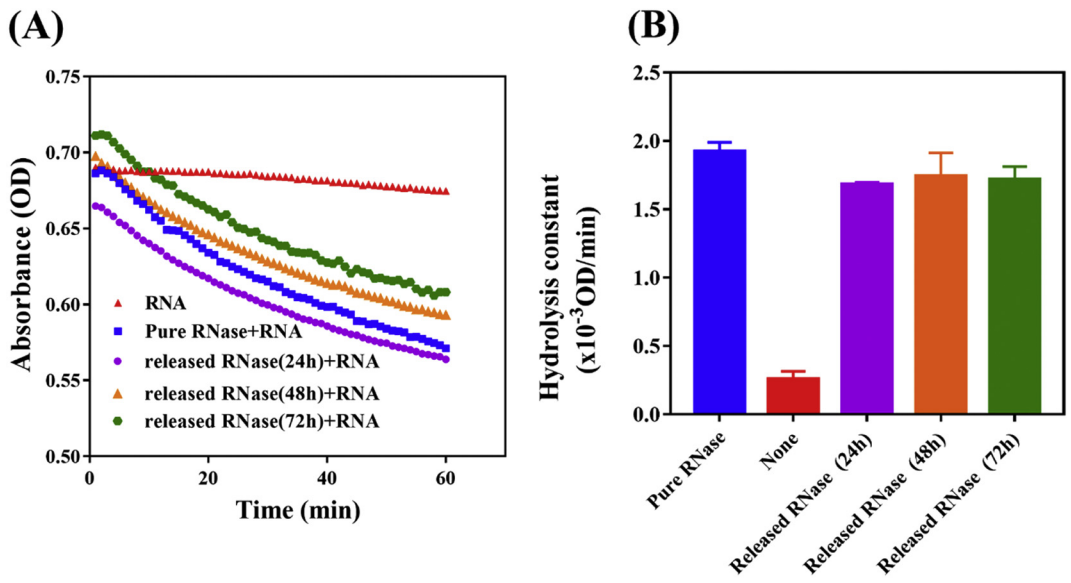

Fig. 5. (A) The absorbance of RNA (3 mg/mL) incubated with pure RNase, released RNase at 24 h, released RNase at 48 h or released RNase at 72 h (0.5–0.75 Kunitz/mL on RNase basis) for 60 min. (B) The hydrolysis constant of pure RNase, released RNase (24 h), released RNase (48 h) and released RNase (72 h).

3.3. Supramolecular nanogels for RNase loading

Inspired by its spontaneous self-assembly in aqueous conditions, RNase was assessed for loading into the nanogels (Fig. 3A). Various ratios of PLG-*g*-mPEG/Azo and PLG-*g*-mPEG/βCD were investigated for protein loading efficiency. When the ratio of PLG-*g*-mPEG/Azo and PLG-*g*-mPEG/βCD were 15:15, the DLC and DLE of RNase reached 23.5% and 50.4%, respectively (Fig. 3B). These results were consistent with the changes in diameter, indicating that the weight ratio of PLG-*g*-mPEG/Azo and PLG-*g*-mPEG/βCD at 15:15 were optimal conditions for RNase loading. Under these conditions, the nanogels had compact cross-linking networks were of a small size. DLS analysis showed that the diameter of nano-RNase at a weight ratio of 15:15 was 134 ± 32 nm and TEM images showed that of nano-RNase were

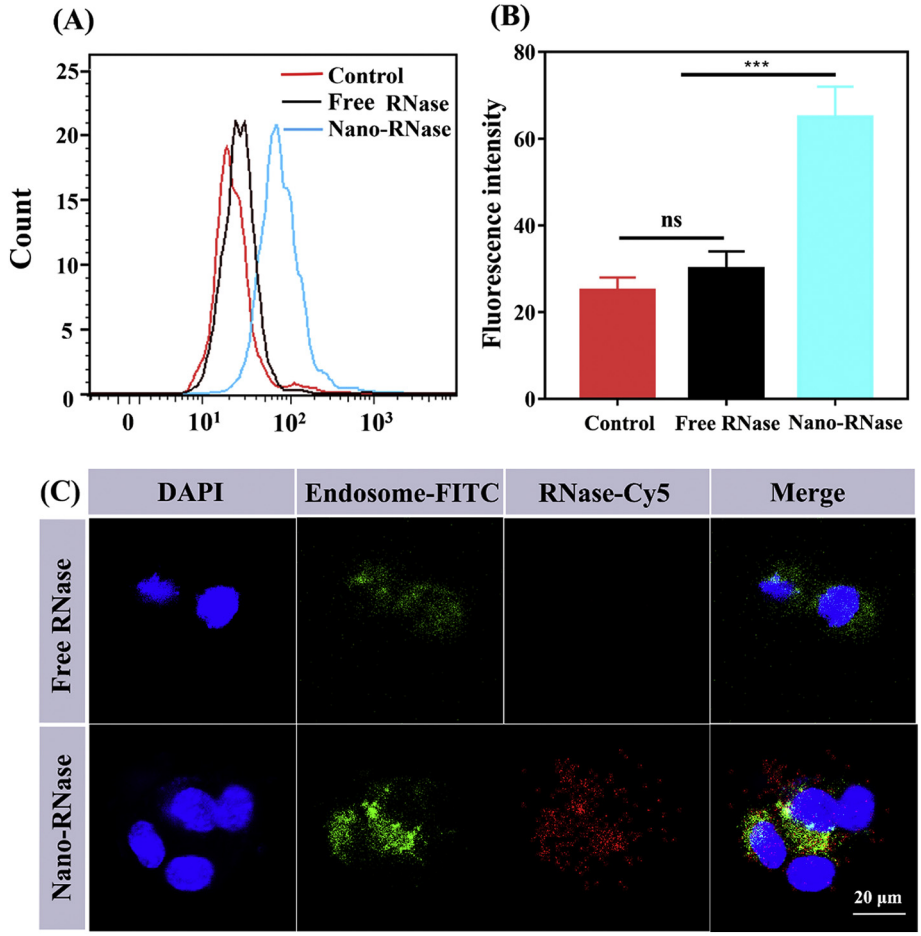

Fig. 6. Internalization of nano-RNase in 4T1 cells. (A) Flow cytometry of 4T1 cells incubated with nano-RNase or free RNase. ($n = 3$) (B) Quantification of Fig. A. ns, not significant. ***$p < .001$ (C) CLSM images of 4T1 cells incubated with nano-RNase or free RNase for 8 h. Scale bar: 20 μm.

95 ± 14 nm (Fig. 3C). To evaluate the stability of the nanogels in PBS, their sizes were measured at predetermined time intervals. As shown in Fig. 3D, the diameter of the nanogels was stable at about 120 nm within 72 h, with no significant size or intensity changes occurring, thereby indicating excellent stability.

The stability of RNase labelled with FITC in the nanogels was measured by fluorescence spectrometry. Briefly, degradation of the FITC-labelled protein results in fluorescence intensity increase because of spreading of FITC [40]. As shown in Fig. S3, the nano-RNase (RNase was labelled with FITC) showed a much slower increase in fluorescence intensity compared to free RNase-FITC. This result demonstrated that the RNase was safely protected from proteolysis by this nanogel.

3.4. Hypoxia-sensitive release of RNase from the nanogels

As shown in Fig. 4A, Azo could be reduced to aniline derivatives under the catalysis of NTR [41]. Since NTR is highly expressed in the hypoxic environment of cancer cells, the nanogels formed by PLG-*g*-mPEG/Azo and PLG-*g*-mPEG/βCD were expected to show hypoxia-sensitive release behaviour [42,43]. To mimic the *in vivo* hypoxic conditions, the release behavior of RNase from nano-RNase was studied *in vitro* in the presence of NTR and NADPH. Release behaviour in PBS was also assessed as a control for normoxic conditions. As shown in Fig. 4B, 75.0 ± 3.5% of RNase was released from the nano-RNase at 72 h under hypoxic conditions, whilst only 19.7 ± 7.4% was released in 72 h under normoxic conditions. Free RNase was released to almost 100% within 12 h, indicating no retardation of RNase in the dialysis tube. The accelerated RNase release in the hypoxic environment suggested the potential of the nanogels for tumor-selective drug delivery and drug release.

The released RNase under each condition was characterized by CD spectroscopy. The peak of the alpha-helix occurred at 208 and 222 nm and the peak of the beta-strand occurred at 218 nm [44]. As shown in Fig. 4C, the circular dichroism spectrum of RNase-FITC was same as free RNase, indicating that the conjugate of FITC had no influence on the secondary structure of RNase. Notably, the RNase peaks under the different conditions were comparable to free RNase, confirming that the secondary structure of the RNase was maintained during the release process.

3.5. The activity of RNase released from the nanogels

Firstly, the activity of released RNase was assessed by Ribonuclease A Detection Kit As shown in Fig. 5, pure RNA has a stable absorbance during 60 min, while RNA incubated with pure RNase could significantly decrease from 0.70 OD to 0.56 OD, suggesting the degradation of RNA. Notably, the released RNase at 24 h, 48 h or 72 h has the same hydrolysis constant as pure RNase, indicating that the activity of released RNase was completely remained. The activity of released RNase was further determined by RNA electrophoresis. As shown in Fig. S4, free RNA has an obvious band, while the band of RNA after incubation with pure RNase and released RNase at different times was not observed, indicating RNA was effectively degraded after incubation with released RNase.

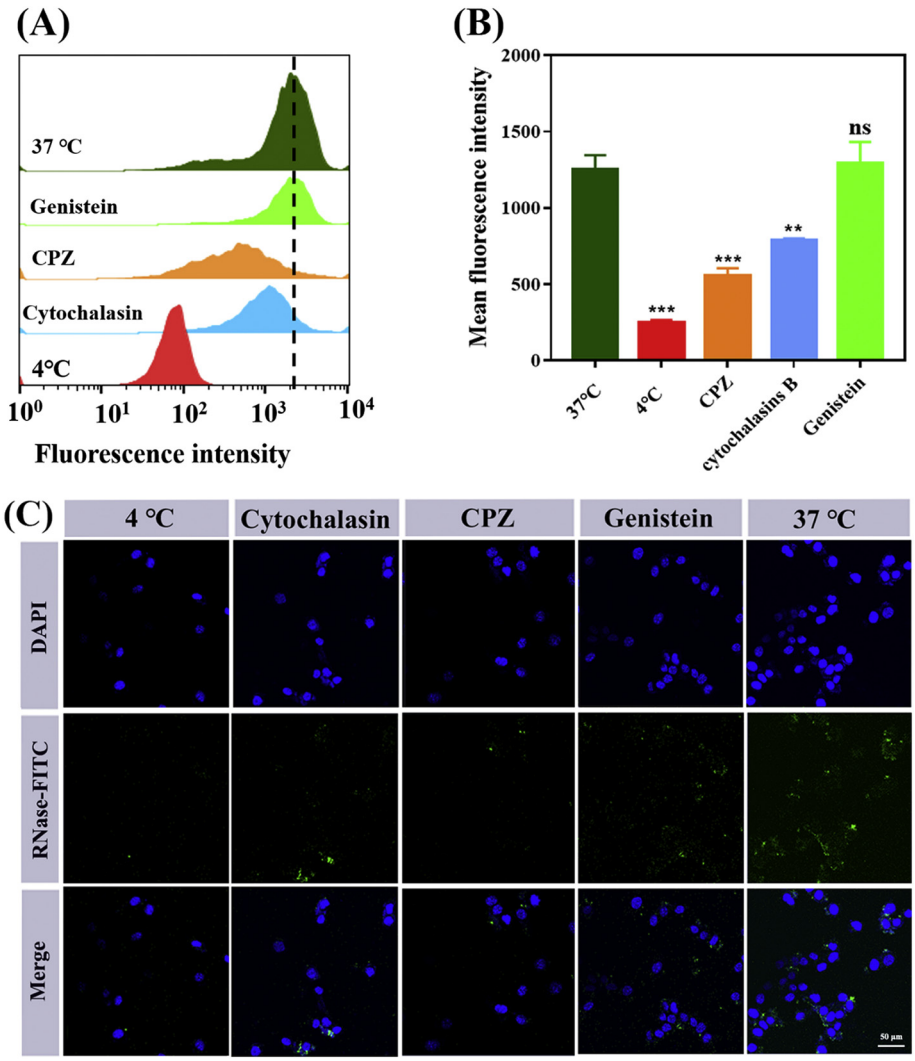

Fig. 7. The internalization pathways of nano-RNase by 4T1 cells. Cells were pre-incubated with inhibitors including the clathrin-mediated endocytosis inhibitor (CPZ) or the macropinocytosis inhibitors (cytochalasin D), the caveolar inhibitors (genistein). . The cells treated with nano-RNase for 4 h were observed. (A) Flow cytometry of 4T1 cells incubated with nano-RNase. ($n = 3$) (B) Quantification of Fig. A. ns, not significant. $^{**}p < .01$,$^{***}p < .001$ (C) CLSM images of 4T1 cells incubated with nano-RNase under different conditions. Scale bar: 50 μm.

3.6. Cellular uptake

The internalization of nano-RNase or free RNase was investigated by flow cytometry and CLSM. Cell nuclei were DAPI labelled and RNase was labelled with Cy5. Lysosomes were stained with lysotracker-FITC. As shown in Fig. 6A-B, after incubation with 4T1 cells for 8 h, the nano-RNase group showed stronger fluorescent intensity (65.4 ± 7.1 a.u.) compared to free RNase treated groups at 8 h (30.7 ± 4.2 a.u.). The results suggested that the nano-RNase could be effectively internalized by 4T1 cells, whilst free RNase could not. To further verify the internalization of nano-RNase by 4T1 cells, nano-RNase or free RNase incubated with 4T1 cells for 8 h was observed by CLSM. CLSM images (Fig. 6C) shown that RNase-FITC alone is membrane impermeable, however, the internalization of nano-RNase is significantly enhanced in the presence of nanogels. In summary, these data indicate that the nanogels effectively increased RNase penetration into 4T1 cells.

3.7. The mechanism of nano-RNase uptake by 4T1 cells

The mechanism of nano-RNase uptake by 4T1 cells were further studied. The results showed that cellular uptake of nano-RNase was much inhibited at 4 °C than 37 °C, and that was moderately inhibited at the role of clathrin-mediated endocytosis inhibitor (CPZ) or the macropinocytosis inhibitors (cytochalasin D), suggesting the internalization of nano-RNase was energy-dependent and involved with multiple pathways including macropinocytosis and clathrin-dependent endocytosis (Fig. 7).

3.8. Cell cytotoxicity

To assess the *in vitro* biocompatibility of the materials, PLG-*g*-mPEG/Azo and PLG-*g*-mPEG/βCD were verified by MTT assays in 4T1 cells. The materials were added into the culture medium at predefined concentrations. As shown in Fig. 8A-B, cell viability was ≥80% after 48 h incubation at concentration ≥ 1000 μg mL^{-1}, suggesting good *in vitro* biocompatibility of the materials.

The antitumor activity of RNase was next investigated *in vitro* through the treatment of 4T1 cells with nano-RNase or free RNase. Nano-RNase was incubated in normoxic (21% O_2 content) or hypoxic (1% O_2 content) conditions. Free RNase was incubated in normoxic conditions. As shown in Fig. 8C-D, free RNase showed low toxicity, minimal internalization into 4T1 cells. In contrast, nano-RNase significantly increased the cytotoxicity of RNase attributed to its enhanced internalization into cells. Notably, we observed that the cytotoxicity

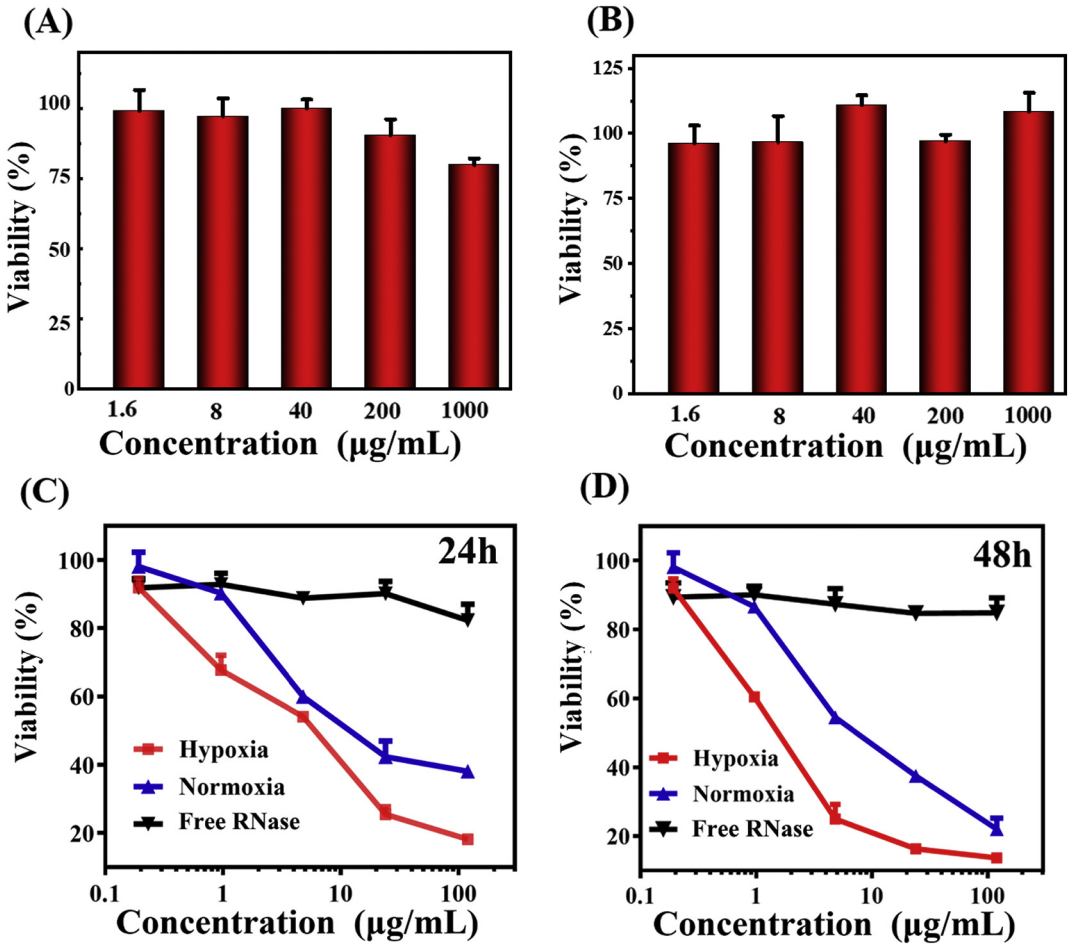

Fig. 8. 4T1 viability of the materials and nano-RNase. *In vitro* cytotoxic of (A) PLG-*g*-mPEG/Azo and (B) PLG-*g*-mPEG/βCD to 4T1 cells at 24 h ($n = 3$). *In vitro* cell viability of 4T1 cells incubated with nano-RNase in hypoxic or normoxic conditions and free RNase in normoxic conditions for (C) 24 h and (D) 48 h ($n = 3$).

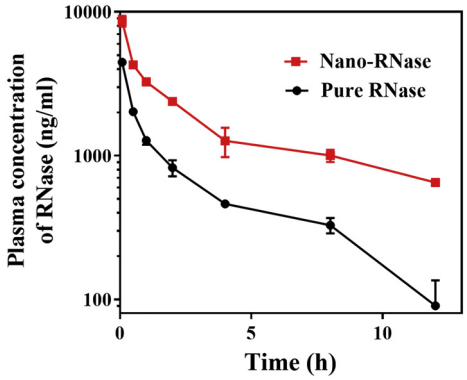

Fig. 9. *In vivo* pharmacokinetic profiles following the intravenous injection of free RNase and nano-RNase. Data are the mean ± standard deviation ($n = 3$).

was markedly enhanced in hypoxic conditions compared to normoxic conditions. After 24 h, the IC_{50} in hypoxic conditions (6.5 μg mL^{-1}) was 2-fold lower than that in normoxic conditions (12.1 μg mL^{-1}). After 48 h, the IC_{50} of nano-RNase in hypoxic conditions (1.7 μg mL^{-1}) was ~4-fold lower than that of normoxic conditions (7.6 μg mL^{-1}). These results indicate that hypoxia induced the increase of NTR and accelerated RNase release. The cell viability of normal cells (NIH-3T3 cells) incubation with nano-RNase was assessed. The results showed that the cell viability of NIH-3T3 cells was all above 80% after 48 h incubation at the concentration as high as 60 μg mL^{-1} (Fig. S5) which is much higher than that in 4T1 tumor cells. The differences should be attributed to the vast difference in intracellular nitroreductase levels between normal cells and tumor cells, and suggest that nano-RNase trigger little RNA degradation in normal cells.

Table 1
Pharmacokinetic parameters estimated for free RNase and nano-RNase in rats.

Types	$t_{1/2}$[a](h)	AUC_{0-t}[b](ng/mL h)	CL[c](mL/h/kg)	Vz[d](mL/kg)
Free RNase	3.17 ± 0.81	7327.88 ± 54.12	5.50 ± 0.51	24.41 ± 5.12
Nano-RNase	6.69 ± 2.08	19,641.74 ± 1409.29	1.50 ± 0.50	15.50 ± 4.11

[a] t1/2z: half-life.
[b] AUC_{0-t}: area under the drug concentration–time curve from 0 to 12 h in plasma.
[c] CL: total body clearance.
[d] Vz: apparent volume of distribution

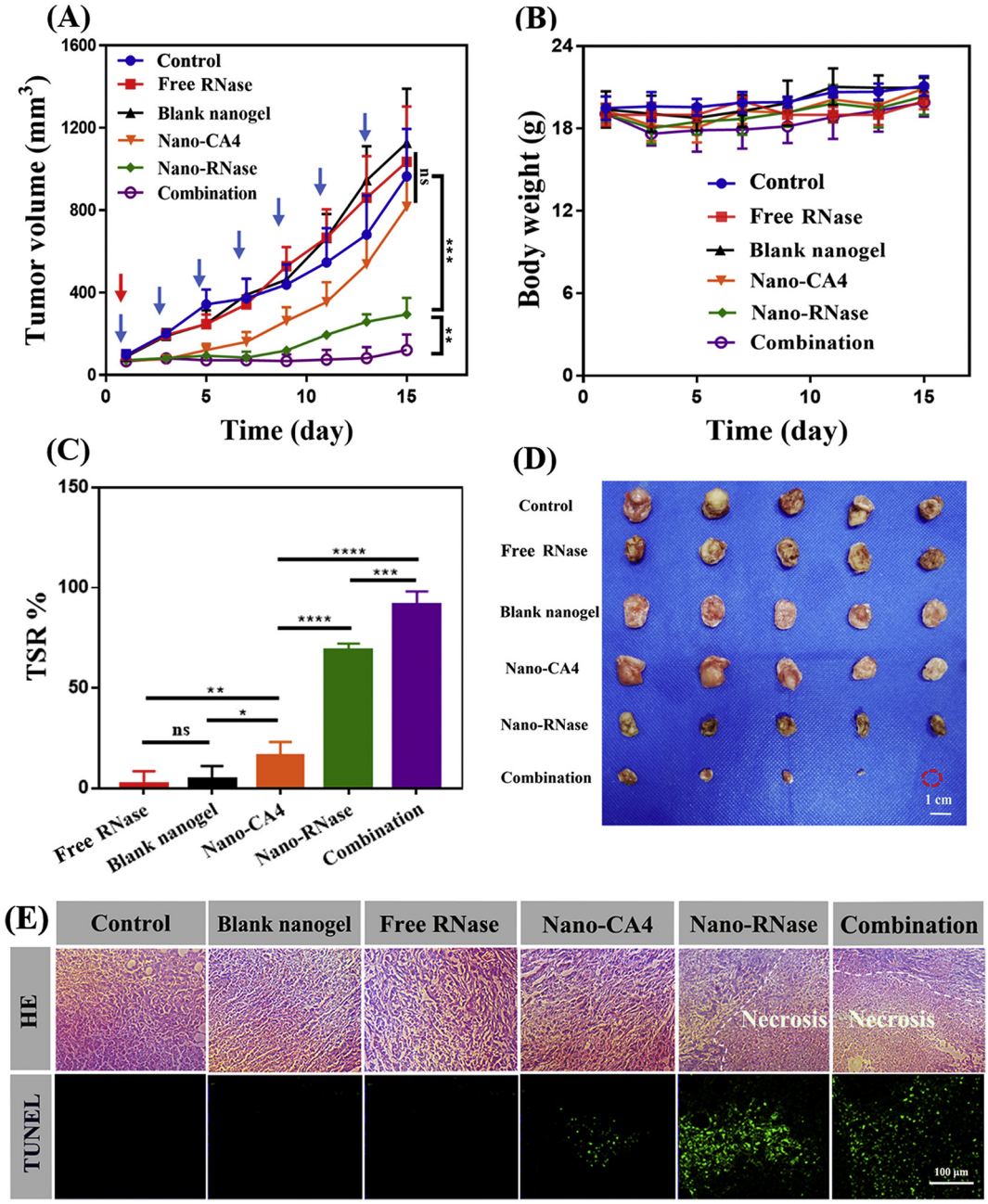

Fig. 10. Nano-CA4 and nano-RNase therapy in 4T1 tumor models. (A) *In vivo* antitumor efficacy of PBS, free RNase (10 mg kg^{-1}), blank nanogels (40 mg kg^{-1}), nano-CA4 (36 mg kg^{-1}, CA4 eq), nano-RNase (10 mg kg^{-1}, RNase eq) and nano-CA4 + nano-RNase (combination group: 36 mg kg^{-1}, CA4 eq; 10 mg kg^{-1}, RNase eq) in 4T1 tumor bearing Balb/C mice ($n = 5$ mice per group). Blue arrows represent nano-RNase injection. Red arrows represent nano-CA4 injection. (B) Body weight changes of 4T1 tumor bearing mice during treatment. (C) TSR% results on day 15. (D) Tumor images after treatment on day 15. (E) H&E and TUNEL staining (scale bar: 100 μm) of tumors from the mice at the end of the treatment period. ns, not significant. *$p < .05$, **$p < .01$, ***$p < .001$, ****$p < .0001$. (For interpretation of the references to colour in this figure legend, the reader is referred to the web version of this article.)

3.9. Pharmacokinetics

Metabolic behaviours of free RNase and nano-RNase in the blood were studied in Wistar rats. As shown in Fig. 9, nano-RNase showed significantly prolonged blood circulation times ($t_{1/2}$ = 6.69 h) compared to free RNase ($t_{1/2}$ = 3.17 h). The remaining RNase concentration of the nano-RNase group was over 600 ng/mL in the blood after 12 h, compared to 90 ng/mL in the free RNase group. As shown in Table 1, the $AUC_{0\text{-}T}$ of the nano-RNase group were 19,641.74 ± 1409.29 ng/mL h, which was obviously higher than that of the free RNase group (7327.88 ± 54.12 ng/mL h). The C_L and V_Z of the nano-RNase group were lower than the free RNase group. These results indicated that the nanogels could reduce the absorption of plasma proteins to RNase, protect the RNase from the reticuloendothelial system (RES) and avoid the loss of RNase in the blood circulation. This was meaningful for the passive accumulation of RNase in tumor tissue due to the EPR effect.

3.10. In vivo anticancer efficacy

Inspired by the release behaviour and the high anti-proliferation effects of the nano-RNase *in vitro*, its antitumor efficacy in 4T1 tumor models was assessed. When the tumors reached a size of ~80 mm^3, mice were randomly divided into 6 groups: PBS, free RNase, blank

nanogel, nano-CA4 (36 mg kg^{-1} on CA4 basis), nano-RNase (10 mg kg^{-1} on RNase basis) and nano-CA4 + nano-RNase (10 mg kg^{-1} on RNase basis and 36 mg kg^{-1} on CA4 basis). Nano-RNase or free RNase were administrated every other day *via* the tail vein. Nano-CA4 was administrated on day 1. Tumor volumes and body weight changes of the 4T1 tumor bearing mice during the treatment period are shown in Fig. 10A-B. Notably, significant tumor inhibition was observed in the nano-RNase group (TSR% 68.7%), whilst the blank nanogels and free RNase showed no obvious tumor inhibition effects (Fig. 10C). These results indicated the nanogels significantly improve the activity of RNase *in vivo*.

Combretastatin A4 (CA4), as a vascular disrupting agent, can disrupt tumor blood vessels and interdict the supply source of oxygen, leading to elevated hypoxia levels in treated tumors. Recently, we reported that CA4 nanomedicines could selectively elevate hypoxia and increase the levels of nitroreductase in treated tumors [45,46]. We therefore hypothesized that nano-CA4 could boost the release of nano-RNase in treated tumors and enhance its antitumor effects. The combination of nano-CA4 and nano-RNase for 4T1 tumor therapy may result in synergistic effects. Tumor growth of the nano-CA4 group was modestly inhibited, with a TSR% of 16.3%. Significantly, the combination of Nano-CA4 and Nano-RNase resulted in a TSR% of 91.7%, consistent with the hypothesis that nano-CA4 accelerates the release of RNase and enhances the therapeutic effects of nano-RNase. The corresponding images of the tumors excised from different treatment groups (Fig. 10D) and tumor weights (Fig. S6) also illustrated that the combination therapy and nano-RNase group showed high antitumor efficiency.

To further evaluate the therapeutic effects, excised tumors at the end of treatment were analyzed by H&E and TUNEL staining. As shown in Fig. 10E, clear nuclei and regular shapes of the tumor cells were observed in PBS, free RNase, blank nanogels or nano-CA4 groups. In contrast, abnormal cell nuclei and differing degrees of tumor tissue necrosis were observed in the nano-RNase and combination groups, indicating that nano-RNase and combination therapy effectively inhibited tumor growth. TUNEL assays showed similar tumor growth inhibition. For systemic toxicity, the average body weights of all groups decreased by < 10.0% during treatment, and no significant necrosis or apoptosis in the organs was observed for all groups (Fig. S7), indicating the safety of nano-CA4 and nano-RNase. Taken together, these data demonstrate that nano-RNase holds potential for protein delivery *in vivo*.

4. Conclusions

In this study, we successfully developed a hypoxia-sensitive nanogel based on host-guest supramolecular interactions between PLG-*g*-mPEG/Azo and PLG-*g*-mPEG/βCD. RNase was encapsulated in the cross-linking network and *in vitro* studies showed that the supramolecular nanogels were of an appropriate size and showed high stability. The RNase could be released under hypoxic conditions. Furthermore, the secondary structure of the released RNase was maintained. The nanogels enhanced cellular uptake and promoted the intracellular release of the cytotoxic RNase. *In vivo* studies showed that nano-RNase significantly prolonged the stability of the RNase in the circulation. The nano-RNase exhibited enhanced antitumor activity compared to free RNase in 4T1 TNBC tumor models with minimal systemic toxicity. When combined with nano-CA4, the hypoxic environment of the tumors accele rated the release of RNase, inhibited tumor growth with a TSR% up to 91.7%. This offers an innovative and efficient strategy for the cytosolic delivery of protein drugs for much needed breast cancer therapies.

Declaration of Competing Interest

The authors declare no competing financial interest.

Acknowledgements

This work was financially supported by the National Natural Science Foundation of China (51673189, 51673185, 51703225, 51833010, 51973215 and 51520105004), Ministry of Science and Technology of China (Project 2018ZX09711003-012), and the Program of Scientific Development of Jilin Province Science (20170101100JC, 20180520207JH, and 20190103112JH).

Appendix A. Supplementary data

Supplementary data to this article can be found online at https://doi.org/10.1016/j.jconrel.2020.01.021.

References

[1] F. Bray, J. Ferlay, I. Soerjomataram, R.L. Siegel, L.A. Torre, A. Jemal, Global cancer statistics 2018: GLOBOCAN estimates of incidence and mortality worldwide for 36 cancers in 185 countries, CA Cancer J. Clin. 68 (6) (2018) 394–424.
[2] A. Bahrami, A. Aledavood, K. Anvari, S.M. Hassanian, M. Maftouh, A. Yaghobzade, O. Salarzaee, S. ShahidSales, A. Avan, The prognostic and therapeutic application of microRNAs in breast cancer: tissue and circulating microRNAs, J. Cell. Physiol. 233 (2) (2018) 774–786.
[3] S. Banerji, K. Cibulskis, C. Rangel-Escareno, K.K. Brown, S.L. Carter, A.M. Frederick, M.S. Lawrence, A.Y. Sivachenko, C. Sougnez, L. Zou, M.L. Cortes, J.C. Fernandez-Lopez, S. Peng, K.G. Ardlie, D. Auclair, V. Bautista-Pina, F. Duke, J. Francis, J. Jung, A. Maffuz-Aziz, R.C. Onofrio, M. Parkin, N.H. Pho, V. Quintanar-Jurado, A.H. Ramos, R. Rebollar-Vega, S. Rodriguez-Cuevas, S.L. Romero-Cordoba, S.E. Schumacher, N. Stransky, K.M. Thompson, L. Uribe-Figueroa, J. Baselga, R. Beroukhim, K. Polyak, D.C. Sgroi, A.L. Richardson, G. Jimenez-Sanchez, E.S. Lander, S.B. Gabriel, L.A. Garraway, T.R. Golub, J. Melendez-Zajgla, A. Toker, G. Getz, A. Hidalgo-Miranda, M. Meyerson, Sequence analysis of mutations and translocations across breast cancer subtypes, Nature 486 (7403) (2012) 405–409.
[4] E.A. Rakha, M.E. El-Sayed, A.R. Green, A.H.S. Lee, J.F. Robertson, I.O. Ellis, Prognostic markers in triple-negative breast cancer, Cancer 109 (1) (2007) 25–32.
[5] W.D. Foulkes, I.E. Smith, J.S. Reis-Filho, Triple-negative breast cancer, N. Engl. J. Med. 363 (20) (2010) 1938–1948.
[6] R. Nanda Saha, Concepts and targets in triple-negative breast cancer: recent results and clinical implications, Ther. Adv. Med. Oncol. 8 (5) (2016) 351–359.
[7] L.A. Emens, C. Cruz, J.P. Eder, F. Braiteh, C. Chung, S.M. Tolaney, I. Kuter, R. Nanda, P.A. Cassier, J.-P. Delord, M.S. Gordon, E. ElGabry, C.-W. Chang, I. Sarkar, W. Grossman, C. O'Hear, M. Fasso, L. Molinero, P. Schmid, Long-term clinical outcomes and biomarker analyses of atezolizumab therapy for patients with metastatic triple-negative breast cancer a phase 1 study, Jama Oncol. 5 (1) (2019) 74–82.
[8] D. Toppmeyer, A.D. Seidman, M. Pollak, C. Russell, K. Tkaczuk, S. Verma, B. Overmoyer, V. Garg, E. Ette, M.W. Harding, G.D. Demetri, Safety and efficacy of the multidrug resistance inhibitor Incel (Biricodar; VX-710) in combination with paclitaxel for advanced breast cancer refractory to paclitaxel, Clin. Cancer Res. 8 (3) (2002) 670–678.
[9] W. Song, L. Shen, Y. Wang, Q. Liu, T.J. Goodwin, J. Li, O. Dorosheva, T. Liu, R. Liu, L. Huang, Synergistic and low adverse effect cancer immunotherapy by immunogenic chemotherapy and locally expressed PD-L1 trap, Nat. Commun. 9 (2018) 2237.
[10] J. Lv, B. He, J. Yu, Y. Wang, C. Wang, S. Zhang, H. Wang, J. Hu, Q. Zhang, Y. Cheng, Fluoropolymers for intracellular and in vivo protein delivery, Biomaterials 182 (2018) 167–175.
[11] W. Song, K. Tiruthani, Y. Wang, L. Shen, M. Hu, O. Dorosheva, K. Qiu, K.A. Kinghorn, R. Liu, L. Huang, Trapping of lipopolysaccharide to promote immunotherapy against colorectal cancer and attenuate liver metastasis, Adv. Mater. 30 (52) (2018) 1805007.
[12] J.E. Lee, R.T. Raines, Ribonucleases as novel chemotherapeutics, Biodrugs 22 (1) (2008) 53–58.
[13] X. Si, W. Song, S. Yang, L. Ma, C. Yang, Z. Tang, Glucose and pH dual-responsive nanogels for efficient protein delivery, Macromol. Biosci. 19 (2019) 1900148.
[14] L.D. Simon, W.N. Charman, S.A. Charman, V.J. Stella, Protein transport across hydrated hyaluronic acid ester membranes: evaluation of ribonuclease a as a potentially useful model protein, J. Control. Release 45 (3) (1997) 273–285.
[15] U. Arnold, R. Ulbrich-Hofmann, Natural and engineered ribonucleases as potential cancer therapeutics, Biotechnol. Lett. 28 (20) (2006) 1615–1622.
[16] J. Lv, Q. Fan, H. Wang, Y. Cheng, Polymers for cytosolic protein delivery, Biomaterials 218 (2019) 119358.
[17] C. Liu, T. Wan, H. Wang, S. Zhang, Y. Ping, Y. Cheng, A boronic acid-rich dendrimer with robust and unprecedented efficiency for cytosolic protein delivery and CRISPR-Cas9 gene editing, Sci. Adv. 5 (6) (2019) eaaw8922.
[18] C. Yu, E. Tan, Y. Xu, J. Lv, Y. Cheng, A Guanidinium-rich polymer for efficient cytosolic delivery of native proteins, Bioconjug. Chem. 30 (2) (2019) 413–417.
[19] J. Zhang, J. Du, M. Yan, A. Dhaliwal, J. Wen, F. Liu, T. Segura, Y. Lu, Synthesis of protein nano-conjugates for cancer therapy, Nano Res. 4 (5) (2011) 425–433.
[20] X.W. Liu, P. Zhang, D.S. He, W.G. Rodl, T. Preiss, J.O. Radler, E. Wagner, U. Lachelt, pH-reversible cationic RNase a conjugates for enhanced cellular delivery and tumor

cell killing, Biomacromolecules 17 (1) (2016) 173–182.
[21] M. Liu, S. Shen, D. Wen, M. Li, T. Li, X. Chen, Z. Gu, R. Mo, Hierarchical nanoassemblies-assisted combinational delivery of cytotoxic protein and antibiotic for cancer treatment, Nano Lett. 18 (4) (2018) 2294–2303.
[22] N. Kordalivand, D. Li, N. Beztsinna, J.S. Torano, E. Mastrobattista, C.F. van Nostrum, W.E. Hennink, T. Vermonden, Polyethyleneimine coated nanogels for the intracellular delivery of RNase A for cancer therapy, Chem. Eng. J. 340 (2018) 32–41.
[23] F.M. Veronese, G. Pasut, PEGylation, successful approach to drug delivery, Drug Discov. Today 10 (21) (2005) 1451–1458.
[24] Z. Zhang, W. Shen, J. Ling, Y. Yan, J. Hu, Y. Cheng, The fluorination effect of fluoroamphiphiles in cytosolic protein delivery, Nat. Commun. 9 (2018) 1377.
[25] R. Dong, Y. Zhou, X. Huang, X. Zhu, Y. Lu, J. Shen, Functional supramolecular polymers for biomedical applications, Adv. Mater. 27 (3) (2015) 498–526.
[26] M.M. Welling, S.J. Spa, D.M. van Willigen, D.D.D. Rietbergen, M. Roestenberg, T. Buckle, F.W.B. van Leeuwen, In vivo stability of supramolecular host-guest complexes monitored by dual-isotope multiplexing in a pre-targeting model of experimental liver radioembolization, J. Control. Release 293 (2019) 126–134.
[27] L. Gao, F. Zabihi, S. Ehrmann, S. Hedtrich, R. Haag, Supramolecular nanogels fabricated via host-guest molecular recognition as penetration enhancer for dermal drug delivery, J. Control. Release 300 (2019) 64–72.
[28] R. Dong, Y. Pang, Y. Su, X. Zhu, Supramolecular hydrogels: synthesis, properties and their biomedical applications, Biomater. Sci. 3 (7) (2015) 937–954.
[29] J.-F. Xu, X. Zhang, Study on supramolecular polymers in China: an overview and outlook, Acta Polym. Sin. 1 (2017) 37–49.
[30] S. Xu, P. Chang, B. Zhao, M. Adeel, S. Zheng, Formation of poly(epsilon-caprolactone) networks via supramolecular hydrogen bonding interactions, Chin. J. Polym. Sci. 37 (3) (2019) 197–207.
[31] X. Chen, Q. Zhong, S. Wang, Y. Wu, J. Tan, H. Lei, S. Huang, Y. Zhang, Progress in dynamic covalent polymers, Acta Polym. Sin. 50 (5) (2019) 469–484.
[32] W. Song, S.N. Musetti, L. Huang, Nanomaterials for cancer immunotherapy, Biomaterials 148 (2017) 16–30.
[33] Y. Liu, H. Wang, K. Kamei, M. Yan, K.-J. Chen, Q. Yuan, L. Shi, Y. Lu, H.-R. Tseng, Delivery of intact transcription factor by using self-assembled supramolecular nanoparticles, Angew. Chem. Int. Edit. 50 (13) (2011) 3058–3062.
[34] A.L. Harris, Hypoxia - a key regulatory factor in tumour growth, Nat. Rev. Cancer 2 (1) (2002) 38–47.
[35] Y. Guan, H.-B. Zhao, L.-X. Yu, S.-C. Chen, Y.-Z. Wang, Multi-stimuli sensitive supramolecular hydrogel formed by host-guest interaction between PNIPAM-Azo and cyclodextrin dimers, RSC Adv. 4 (10) (2014) 4955–4959.
[36] Y. Zhang, M. Huo, J. Zhou, S. Xie, PKSolver: an add-in program for pharmacokinetic and pharmacodynamic data analysis in Microsoft excel, Comput. Methods Prog. Biomed. 99 (3) (2010) 306–314.
[37] G. Chen, B. Ma, R. Xie, Y. Wang, K. Dou, S. Gong, NIR-induced spatiotemporally controlled gene silencing by upconversion nanoparticle-based siRNA nanocarrier, J. Control. Release 282 (2018) 148–155.
[38] C. Namasivayam, D. Kavitha, IR, XRD and SEM studies on the mechanism of adsorption of dyes and phenols by coir pith carbon from aqueous phase, Microchem. J. 82 (1) (2006) 43–48.
[39] A. Harada, Cyclodextrin-based molecular machines, Acc. Chem. Res. 34 (6) (2001) 456–464.
[40] J.E. Chung, S. Tan, S.J. Gao, N. Yongvongsoontorn, S.H. Kim, J.H. Lee, H.S. Choi, H. Yano, L. Zhuo, M. Kurisawa, J.Y. Ying, Self-assembled micellar nanocomplexes comprising green tea catechin derivatives and protein drugs for cancer therapy, Nat. Nanotechnol. 9 (11) (2014) 907–912.
[41] G. Yang, S.Z.F. Phua, W.Q. Lim, R. Zhang, L. Feng, G. Liu, H. Wu, A.K. Bindra, D. Jana, Z. Liu, Y. Zhao, A hypoxia-responsive albumin-based nanosystem for deep tumor penetration and excellent therapeutic efficacy, Adv. Mater. 31 (25) (2019) 1901513.
[42] F.S. Nouri, X. Wang, A. Hatefi, Genetically engineered theranostic mesenchymal stem cells for the evaluation of the anticancer efficacy of enzyme/prodrug systems, J. Control. Release 200 (2015) 179–187.
[43] Z. Liu, F. Song, W. Shi, G. Gurzadyan, H. Yin, B. Song, R. Liang, X. Peng, Nitroreductase-activatable theranostic molecules with high PDT efficiency under mild hypoxia based on a TADF fluorescein derivative, ACS Appl. Mater. Interfaces 11 (17) (2019) 15426–15435.
[44] R.W. Janes, PDB2CD visualises dynamics within protein structures, Eur. Biophys. J. 46 (7) (2017) 607–616.
[45] S. Yang, Z. Tang, C. Hu, D. Zhang, N. Shen, H. Yu, X. Chen, Selectively potentiating hypoxia levels by combretastatin A4 nanomedicine: toward highly enhanced hypoxia-activated prodrug tirapazamine therapy for metastatic tumors, Adv. Mater. 31 (11) (2019) 1805955.
[46] N. Shen, J. Wu, C. Yang, H. Yu, S. Yang, T. Li, J. Chen, Z. Tang, X. Chen, Combretastatin A4 nanoparticles combined with hypoxia-sensitive imiquimod: a new paradigm for the modulation of host immunological responses during cancer treatment, Nano Lett. (2019) 8021–8031.